Solar Energy Materials & Solar Cells 269 (2024) 112761

Contents lists available at ScienceDirect

Solar Energy Materials and Solar Cells

journal homepage: www.elsevier.com/locate/solmat

Mn and Al co-modified CaO-based composites from various calcium precursors for thermochemical energy storage: High energy storage density and excellent solar absorption ability

Fengyuan Chai [a,b,1], Peiwang Zhu [a,b,c,1], Haoran Xu [a,b,c], Xiangyu Xie [a,b], Gang Xiao [a,b,c,*]

[a] Key Laboratory of Clean Energy and Carbon Neutrality of Zhejiang Province, Zhejiang University, Hangzhou, Zhejiang, 310027, China
[b] State Key Laboratory of Clean Energy Utilization, Zhejiang University, 38 Zheda Road, Hangzhou, 310027, China
[c] Jiaxing Research Institute, Zhejiang University, 1300 Dongshengxilu Road, Jiaxing, 314031, China

ARTICLE INFO

Keywords:
Calcium looping
Thermochemical energy storage
Cycling stability
Solar energy absorption
Density functional theory

ABSTRACT

Thermochemical energy storage (TCES) materials driven by calcium looping (CaL) have great potential to be used in the next generation of concentrated solar power (CSP) plants. However, natural calcium-based materials are easily sintered at high temperatures, and their optical absorption capacities are too low to be directly utilized. To overcome these challenges, Mn and Al co-modified CaO-based composites were developed by the sol-gel method in this work, and three kinds of precursors (calcium acetate, calcium gluconate, and calcium nitrate) were chosen as calcium sources. Considering the energy storage density and the average solar absorption ability, the appropriate doping ratio was determined to be Ca: Mn: Al = 100: 8: 8. In different calcium precursors, the sample fabricated from calcium gluconate forms a stable skeleton and keeps a porous structure during cycles, and its average optical absorption reaches 86.14%. The conversion rate of CaO is maintained at 91.50% over 60 cycles, while that of pure CaO prepared by commercial $CaCO_3$ is only 16.93%. The effect of Mn and Al on the carbonation stage was analyzed by density functional theory (DFT). The CO_2 adsorption energies of the perfect CaO surface and the defective CaO surface co-doped with Mn and Al were calculated. It is found that the defective surface is easier to combine with CO_2, and the generated C-O bond is strengthened. This work develops a doping strategy for outstanding CaO-based composites and explores the physical mechanism of doping elements for enhancing CaO capability from the microscopic aspect.

1. Introduction

As a kind of abundant renewable source, solar energy can effectively replace fossil energy and solve the environmental problems caused by carbon emissions [1]. Among the various technologies of solar energy utilization, concentrated solar power (CSP) systems combined with thermochemical energy storage (TCES) technology can avoid intermittent and fluctuating problems by transforming solar energy into thermal energy and then converting it into electricity [2]. At present, the CSP plants have been developed for the 2nd generation, adopting molten salt as the working medium, whose working temperatures are lower than 565 °C because of the decomposition and corrosion problem [3,4]. According to the Carnot theorem, higher operating temperatures are beneficial to improve thermal efficiency. The next generation CSP plants will pursue higher operating temperatures (>700 °C) and power generation efficiency. The previous working mediums (such as heat-conduction oil and molten salts) cannot withstand high temperatures over 700 °C and their energy storage density is too low to adapt to strict thermal energy storage requirements, so it is essential to select heat storage materials with higher operating temperatures (>700 °C) for the next generation CSP plants [5]. The working temperature of the TCES system based on calcium looping (CaL) is above 700 °C [6], and the energy storage density is up to 3.26 GJ/m^3 [7,8]. The system completes the storage and release of thermal energy by the reversible reaction (Eq. (1)) of $CaO/CaCO_3$, which sufficiently meets the requirements of the 3rd generation CSP plants. The schematic diagram of the 3rd generation CSP plant containing a TCES system driven by calcium looping is shown in Fig. S1.

* Corresponding author. Key Laboratory of Clean Energy and Carbon Neutrality of Zhejiang Province, Zhejiang University, Hangzhou, Zhejiang, 310027, China.
E-mail address: xiaogangtianmen@zju.edu.cn (G. Xiao).
[1] These authors contributed equally to this paper.

https://doi.org/10.1016/j.solmat.2024.112761
Received 15 August 2023; Received in revised form 10 January 2024; Accepted 16 February 2024
Available online 21 February 2024

$$CaO + CO_2 \rightleftharpoons CaCO_3 \quad \Delta H = -178\ kJ/mol \tag{1}$$

Before the large-scale application of the TCES system driven by CaL in the next-generation CSP plants, there are still several key problems to be solved for calcium-based heat storage materials. Firstly, the most prominent problems are serious sintering and poor solar absorption capacity [9], which affect the sustainability and efficiency of calcium-based materials for heat collection under solar light. Doping is a common method to solve the problems of sintering and poor solar absorption capacity. To solve the sintering problem of calcium-based materials, some oxides with high Taman temperatures are incorporated into CaO or $CaCO_3$, such as Al_2O_3 [10–12], SiO_2 [13,14], ZrO_2 [15], MgO [16–18], Y_2O_3 [19], etc. Taking Al_2O_3 as an example, Ammendola and Raganati et al. [20,21] have found that Al_2O_3 is suitable as a sintering inhibitor for carbonate systems and a flow conditioner, and synthesized heat storage composites with excellent performance. For the problem of poor solar absorption of calcium-based materials, some elements that can improve the absorption rate are also incorporated into CaO or $CaCO_3$, such as Mn [22–27], Fe [23,27], Cu [28], Co [29], Cr [30], etc. Zheng et al. [28] studied the effect of various elements on the absorption ability of $CaCO_3$. They found that the Cu element increased the absorption rate in the visible range, but in the near-infrared range, it had little change. Further doping of Co or Cr achieved the promotion of optical absorption on the full spectrum.

Another key issue is the atmosphere and temperature conditions of calcium-based materials in the process of utilization. The CSP-TCES system based on calcium looping has two different integration schemes at the calcination stage [31–33]. One is an open-loop or semi-open-loop system that uses an inert atmosphere such as N_2 or He for calcination. This system has mild calcination conditions and can reduce the sintering of calcium-based materials. However, the CO_2 produced by calcination will be mixed with the inert atmosphere. Although CO_2 can be separated by membrane separation technology [34], it will inevitably increase the cost of the system. In the research of the open-loop system, Liu et al. [24] and Da et al. [30] researched direct solar-driven calcium-looping thermochemical energy storage. The calcination process is carried out in an inert atmosphere and the carbonation process is carried out in CO_2 under the focused sunlight from two Xe lamps. They proved that the modified calcium-based composite has excellent performance in an open-loop system. The other is a closed-loop system using pure CO_2 flow or a mixed atmosphere of CO_2 and N_2 for calcination. The system ensures that the calcination atmosphere is consistent with the carbonation atmosphere, eliminating the step of gas separation and saving costs. However, compared with the open-loop system or semi-open-loop system, the harsh conditions of the closed-loop system also enhance the sintering of calcium-based materials. In the research of the closed-loop system, Luo et al. [35,36] synthesized outstanding CaO-based composites suitable for the closed-loop system and improved the energy storage performance of CaO in the closed-loop system by means of organic acid modification and alkali salt doping. Up to date, the discussion on the applicability of open-loop systems and closed-loop systems has not stopped. In the future, the economics and sustainability of the two systems need to be compared in detail.

Processing the above key problems is necessary before the utilization of the TCES system driven by CaL. In the current research works on the doping of CaO-based heat storage materials, most of them [19,26,37] are to select one kind of precursor for doping to synthesize a composite, and then to study its absorption capacity and cyclic performance. Few works focus on the effect of different calcium precursors on the thermal storage properties of composites. Different calcium precursors undergo diverse microscopic processes and generate different pores and skeleton structures in the synthesis of calcium-based composites [38], which will directly affect the long-term cyclic performance of the materials. Therefore, it is necessary to carry out a study and comparison of various calcium precursors to provide more choices for the synthesis of CaO-based heat storage materials. In an open-loop system or semi-open-loop system, few works consider the influence of temperature and CO_2 partial pressure on the material at the same time. Therefore, it is necessary to carry out relevant research to study the influence of temperature and atmosphere on the performance of synthesized composites.

Hence, we chose three common calcium precursors (calcium acetate, calcium gluconate, and calcium nitrate) to synthesize the CaO-based composites co-doped with Mn and Al. The addition of Al element in CaO delays the sintering under high temperatures, and the addition of Mn element improves the solar absorption rate of the composites. At the beginning of the experiment, the cyclic performance of the control sample was studied in an open-loop system and closed-loop system to explore the more suitable cycle mode (atmosphere, carbonation temperature, and calcination temperature). The mechanism of Mn and Al elements promoting the carbonation reaction after doping was explained using density functional theory (DFT) calculations. The calcium-based precursor with excellent long-term cycle performance was screened out, which provided a reference for the development of calcium-based thermal storage materials, and could also find potential powder precursors for the preparation of calcium-based thermal storage particles.

2. Experimental and computational section

2.1. Materials and synthesis method

Calcium nitrate tetrahydrate (CN, Sinopharm Chemical Reagent Co., ≥98.5%), calcium gluconate monohydrate (CG, Sinopharm Chemical Reagent Co., ≥99.0%), calcium acetate (CA, Shanghai Macklin Biochemical Co., Ltd., ≥96.0%), aluminum nitrate nonahydrate (Sinopharm Chemical Reagent Co., AR, ≥99.0%), manganese nitrate solution (Shanghai Macklin Biochemical Co., Ltd., 50 wt% in H_2O), ethylene glycol (Shanghai Macklin Biochemical Co., Ltd., AR, ≥98.0%), and citric acid (Shanghai Macklin Biochemical Co., Ltd., AR, ≥99.5%) were directly used in the formation of the doped materials without further purification.

The CaO-based materials co-doped with Mn and Al were synthesized by the sol-gel method. In the process of sample preparation, nitrate salts, different calcium precursors, and citric acid were first dissolved in deionized water, where the molar ratio of total metal cations to citric acid was 1:1. The mixed solution was stirred at 70 °C for 3 h. Afterward, ethylene glycol (EG) was added to the mixed solution with the molar ratio of citric acid: ethylene glycol = 3:2 and then kept stirring at 90 °C for 2 h until the viscous gel formed. The gel was dried at 230 °C for 3 h and finally calcined in a chamber furnace at 450 °C for 1 h and 850 °C for 1 h in an air atmosphere. The products were ground and then collected for the following tests.

The whole process is schematically displayed in Fig. 1. The CaO-based composites using different precursors are labeled as CX-Y, where CX represents the calcium precursor (CA, CG, CN) and Y means the molar ratio of Mn/Al to Ca in the composites (refer to Ca as 100). For instance, CA-8 denotes that the calcium precursor is calcium acetate, and the molar ratio of Ca: Mn: Al is 100:8:8. The control sample was made from directly calcined commercial $CaCO_3$ at 450 °C for 1 h and 850 °C for 1 h, which is labeled as pure CaO.

2.2. Characterization techniques

All samples used a PANalytical B.V. X-pert powder diffractometer (Cu Kα radiation) to carry out the analysis of the crystal phase. The range of diffraction angle (2θ) was 10-70° with a step of 0.02° and 30 s counting time per angle, and the results were analyzed using the ICCD PDF-4 database. The X-ray photoemission spectroscopy (XPS) was examined on a Thermo Scientific K-Alpha with a monochromatic Al Kα radiation source (hν = 1486.6 eV). The Bruker EMXplus electron

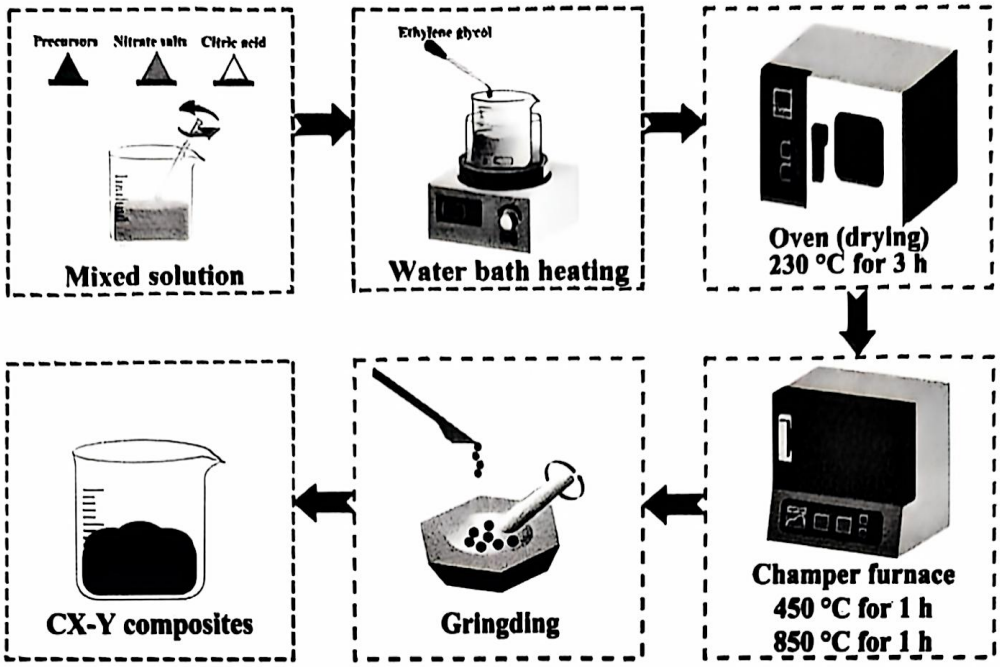

Fig. 1. The processes of sample preparation.

paramagnetic resonance (EPR) spectrometer was employed to examine the oxygen vacancies. The particle size distributions of samples were measured by a Malvern Zetasizer Nano ZS90. The images of scanning electron microscope (SEM) were obtained by a SU8010 field emission scanning electron microscope to investigate the morphology and microstructure. Transmission electron microscopy (TEM) images were obtained from a Tecnai G2 F20 S-TWIN to identify the morphology after cycles. The surface area and porosity were analyzed by an ASAP2460 (Micromeritics). After that, the Brunauer-Emmett-Teller (BET) equation and the Barrett-Joyner-Halenda (BJH) equation were used to get the specific surface area and pore diameter distributions.

The solar absorption abilities of samples were determined by the weighted integral of the optical absorption ratio and the solar spectral irradiance. In the wavelength range of 380-2500 nm, the average optical absorption could be described as:

$$A_{aw} = \frac{\int_{380nm}^{2500nm} \alpha(\lambda) I(\lambda) d\lambda}{\int_{380nm}^{2500nm} I(\lambda) d\lambda} \tag{2}$$

where $\alpha(\lambda)$ and $I(\lambda)$ represent the optical absorption and the standard irradiance of the AM1.5 solar spectrum. The UV–visible–NIR spectrometer (UV3600, Shimadzu) was used to measure the absorption data.

2.3. Cycling stability test

The cycling stability and the heat storage density of samples were monitored via a TGA/DSC3+ simultaneous thermal analyzer (Mettler Toledo) by measuring the change of weight and temperature with time. 10–15 mg of the sample was laid in an alumina crucible to carry out the carbonation and calcination process. The temperatures of the carbonation stage and the calcination stage were kept constant for 10 min. In the meantime, the gas flow rate was fixed at 100 mL/min. The specific temperatures and atmosphere conditions will be further discussed below. To compare the performances of different samples, the conversion rate of CaO (X_N) and heat storage density (D_N, kJ/kg) are expressed as:

$$X_N = \frac{m_{car,N} - m_{cal,N}}{m_0 \cdot w} \cdot \frac{W_{CaO}}{W_{CO_2}} \tag{3}$$

$$D_N = \frac{1000 \cdot (m_{car,N} - m_{cal,N}) \cdot \Delta H}{W_{CO_2} \cdot m_0} \tag{4}$$

where m_0, $m_{car,N}$, and $m_{cal,N}$ refer to the initial mass of the sample, the mass of the sample after the Nth carbonation, and the Nth calcination, respectively. W_{CaO} and W_{CO_2} denote the molar masses of CaO (56 g/mol) and CO_2 (44 g/mol). w means the mass fraction of the effective component (CaO) in the composites. The relevant explanation for w can be found in the supporting information and its value is summarized in Table S1. ΔH is the standard reaction enthalpy of CaO during the stage of carbonation (178 kJ/mol).

2.4. DFT calculation

All of the DFT calculations were operated by the CASTEP (Cambridge Serial Total Energy Package) module of Materials Studio 2019 [39]. The Generalized Gradient Approximation (GGA) and Perdew-Burke-Ernzerhof (PBE) functions were used to optimize the geometry [40]. The interactions between the valence electrons and the cores were calculated using an OTFG ultrasoft pseudopotential. The convergence parameters of the geometry optimization were set as 1.0×10^{-6} Ha (the maximum change of energy), 0.002 Ha/Å (the maximum force), 0.005 Å (the maximum displacement), and 1.0×10^{-6} Ha (the self-consistent field, SCF). The cut-off energy was set to be 700 eV. The sampling method for the Brillouin zone was the Monkhorst-Pack grid of $4 \times 4 \times 1$.

To verify the accuracy of the DFT calculations, the lattice parameter of CaO after geometric optimization had been calculated (4.832 Å), which was close to the experimental data (4.811 Å) [41]. According to previous research [42], the most stable surface of CaO was the (100) surface, and therefore the low-index (100) surface was employed to represent the adsorption surface. A three-dimensional CaO (100) slab with a periodic (3×3) supercell was created and a vacuum region of 15 Å thickness was set to avoid interactions between slabs. All models ensured that the bottom two layers were fixed, and the upper layers and the adsorbate were relaxed.

For the crystal structures of CaO and CaO co-doped with Mn and Al, the adsorption energy characterizes the degree of interaction between

the adsorbate and the substrate, which is shown as:

$$E_{ads} = E_{system} - (E_{substrate} + E_{adsorbate}) \quad (5)$$

where, E_{system} is the total energy of the combination of the adsorbate and the substrate, $E_{substrate}$ means the energy of the substrate, and $E_{adsorbate}$ represents the energy of the adsorbate (i.e., CO_2). E_{ads} is a negative value. The configuration becomes more stable and the combination with CO_2 becomes easier with the value of E_{ads} decreasing [43].

3. Results and discussion

3.1. Analysis of the cyclic temperatures and carbonation atmosphere

The degree of conversion between CaO and $CaCO_3$ depends on the reaction temperature and CO_2 partial pressure. To determine the optimal reaction temperature and carbonation atmosphere, the equilibrium curve of the reversible reaction (Eq. (1)) was obtained by the Van't Hoff equation and the standard molar generation enthalpies and entropies. The result is shown in Fig. 2 (a).

Pure CaO was selected to carry out the conversion tests at diverse temperatures and atmospheres. Firstly, the different reaction temperatures were compared in a fixed atmosphere of CO_2 for carbonation and N_2 for calcination. Five temperature couples (i.e., carbonation temperature – calcination temperature) were selected: 750 °C–750 °C, 750 °C–800 °C, 800 °C–800 °C, 800 °C–850 °C, and 800 °C–900 °C. As shown in Fig. 2 (b), pure CaO behaved the best cyclic performance during 20 cycles in the temperature couple of "750 °C–750 °C". The order of conversion rates in five temperature couples is 40.18%, 36.08%, 34.61%, 29.41%, and 27.18% after 20 cycles, respectively. It indicates that higher operating temperatures aggravate the sintering of CaO. According to the temperature demands of the 3rd generation CSP plants, 750 °C is suitable as the temperature of carbonation and calcination, which will be proper for power generation mode with low collector temperature.

Before determining the calcination atmosphere, the reaction temperature was fixed at 850 °C. As shown in Fig. 2(a), the selection range of the calcination atmosphere is broader at this temperature. The calcination atmosphere was set as "100% N_2", "70% N_2 + 30% CO_2", and "50% N_2 + 50% CO_2". The carbonation atmosphere was fixed at CO_2. The performance of pure CaO over 20 cycles is depicted in Fig. 2(c). The conversion rates in the three types of calcination atmospheres are 27.18%, 19.74%, and 14.45% after 20 cycles, respectively. It suggests that reducing the CO_2 partial pressure promotes the degree of calcination reaction and enhances the conversion activity of $CaCO_3$/CaO. Then, the calcination atmosphere was fixed to N_2 and the temperature was fixed at 750 °C. The effect of the carbonation atmosphere with diverse CO_2 partial pressures on the cyclic performance of pure CaO was studied. It can be seen from Fig. 2 (a) that when the temperature is fixed at 750 °C, the partial pressure of CO_2 must be at least greater than 20 % to carry out the carbonation reaction, so the carbonation atmosphere is set as 100% CO_2, 70% CO_2 + 30% N_2, 50% CO_2 + 50% N_2, 30% CO_2 + 70% N_2. The order of conversion rates in four kinds of carbonation atmospheres is 40.18%, 35.54%, 33.21%, and 22.43% after 20 cycles, respectively. The performance of pure CaO decreases sharply from the fifth cycle under the condition of 30% CO_2 + 70% N_2. It demonstrates that only a little CO_2 passes through the $CaCO_3$ layer on the surface and enters the interior to react with CaO during carbonation. Increasing the CO_2 partial pressure is beneficial to promote the mass transfer process.

The performance tests of pure CaO at three temperature couples were carried out under fixed carbonation and calcination atmospheres (i.e., 80% CO_2 +20% N_2). Under conditions of 650 °C–850 °C, 700 °C–900 °C, and 750 °C–950 °C, respectively, the CaO conversion rate falls to 24.25%, 23.13%, and 23.05% after 20 cycles. As mentioned in the

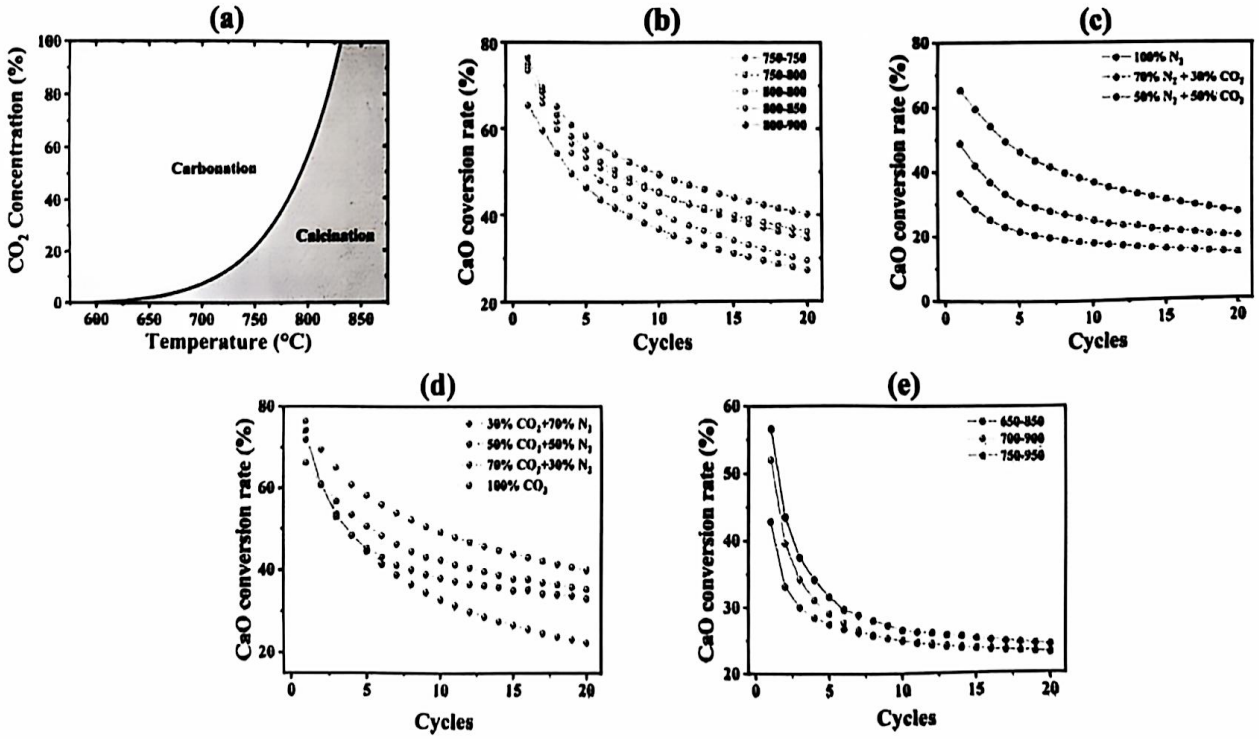

Fig. 2. Determination of the working temperature and atmosphere. (a) The relationship between equilibrium temperature and CO_2 concentration. (b) The evolution of the conversion rate of pure CaO under various temperature modes (atmosphere: carbonation/CO_2; calcination/N_2). (c) The evolution of the conversion rate of pure CaO under various calcination atmosphere modes (temperature: carbonation/850 °C; calcination/850 °C). (d) The evolution of the conversion rate of pure CaO under various carbonation atmosphere modes (temperature: carbonation/750 °C; calcination/750 °C). (e) The evolution of the conversion rate of pure CaO under various temperature modes (fixed atmosphere: 80% CO_2 +20 % N_2).

introduction, the closed-loop system will increase the sintering of Ca-based materials but also eliminate the cost and step of gas separation. In the future, the applicability and economics of open-loop systems and closed-loop systems need to be discussed in depth. To facilitate the comparison of different calcium precursors, the temperatures of subsequent tests were fixed at 750 °C in the atmosphere of CO_2 for carbonation and N_2 for calcination.

3.2. Analysis of the CaO-based composites with different doping ratios

In order to determine the optimal doping ratio, three samples with different doping ratios were synthesized on the basis of calcium gluconate, namely CG-6/CG-8/CG-10. The XRD patterns indicate that CaO (ICCD 97-009-0486) is the major phase as shown in Fig. 3(a). In the meantime, a small amount of $CaMn_2O_4$ (ICCD 97-009-6243), $Ca_3Mn_2O_7$ (ICCD 97-005-5667), and $Ca_3Al_2O_6$ (ICCD 97-015-1369) are formed, demonstrating that the doped Mn and Al elements react with Ca to generate the new oxides, whose peaks become more pronounced as the doping ratio increases. The main diffraction peaks for the doped samples have a slight shift compared to the standard peak for CaO (ICCD 97-009-0486) in Fig. 3(b), indicating that a few Mn and Al atoms come into the CaO lattice. They substitute Ca atoms and contribute to the lattice distortion, causing a difference in the diffraction peak. As shown in Table S2, the lattice parameters of CaO are changed after doping, which indicates that the hetero elements (i.e., the Mn element and the Al element) are inserted into the CaO lattice. At the same time, Fig. S2 shows that the signal of oxygen vacancies in the doped samples is enhanced compared with pure CaO. It demonstrates that the lattice induces the formation of oxygen vacancies. It can also be observed in Fig. 3 (b) that the full width at half maximum (FWHM) of the CG-6 sample is smaller than that of CG-8 and CG-10 samples, implying that with the increment of doped Mn and Al, the extent of the lattice defect will increase [44].

Fig. 4 illustrates the cyclic performances of CG-6, CG-8, and CG-10 samples in the first 20 cycles. The CG-8 sample performs more stable than the CG-6 and CG-10 samples, whose heat storage density decreases slightly in the first few cycles, and then rises steadily as shown in Fig. 4 (b). Specifically, the heat storage density of the CG-8 sample increased by 2.46% to 1955.12 kJ/kg. The phenomenon that cyclic performance is enhanced with increasing cycles has been designated as self-reactivation. It can be explained by the pore-skeleton model proposed by Manovic et al. [45]. During cycling, the diffusion of ions in the CaO crystal is strengthened, and an internal skeleton is gradually formed. With the synergistic effect of the macroscopic skeleton formed by the mass transfer and diffusion of CO_2, the skeleton structure remains steady, protecting the porous structure of the particles and improving the conversion of CaO. It indicates that under the current test conditions, the CG-8 sample may form a more stable skeleton structure than other samples. The heat storage density of the CG-6 sample dropped by 11.33%, reaching 1813.93 kJ/kg and that of the CG-10 sample slightly decreased to 1639.26 kJ/kg over 20 cycles. It implies that a lower doping ratio is inferior to a higher one in cycling stability, but the excessive doping ratio will reduce the mass fraction of the effective component (i.e., CaO), resulting in a decrease in the heat storage density. Meanwhile, the optical absorption of the CG-8 sample is significantly higher than that of the CG-6 sample and slightly lower than that of the CG-10 sample as shown in Fig. S3. Therefore, the following studies fix the doping ratio as Ca: Mn: Al = 100:8:8.

3.3. Analysis of the CaO-based composites with different calcium precursors

After determining the doping ratio, relative characterization and tests were carried out to evaluate samples fabricated from different calcium precursors. The following researches focused on the cycling stability, the optical absorption on the full spectrum, and the micromorphologies.

3.3.1. Characterization of the as-synthesized materials

As seen in Fig. 5, CaO is the main phase of all samples. In the diffraction angle range of 33°–35°, the CaO-based composites prepared from three calcium precursors have different compositions. $CaMn_2O_4$, $Ca_3Mn_2O_7$, and $Ca_3Al_2O_6$ are similar phases in the three doped samples. In addition, the CN-8 and CG-8 samples have a common diffraction peak, namely $CaMnO_3$ (ICCD 97-018-2823). For the CA-8 sample, except for the same phases as CG-8 and CN-8 samples, there is an additional phase

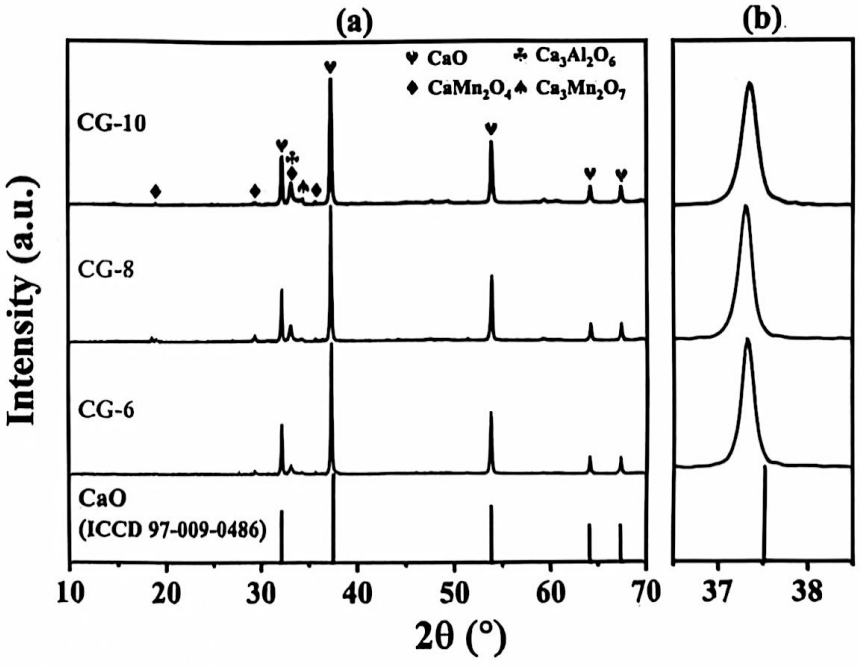

Fig. 3. The XRD patterns of CG-6, CG-8, and CG-10 samples.

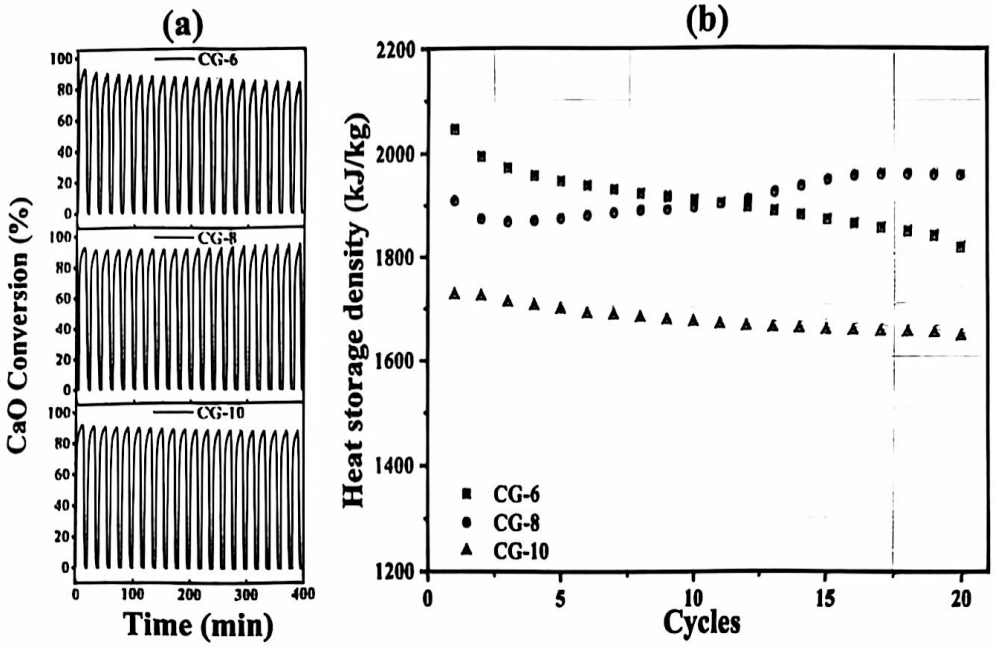

Fig. 4. The cycling stability results. (a) The CaO conversion of the CG samples in the first 20 cycles. (b) The heat storage density of the CG samples in the first 20 cycles.

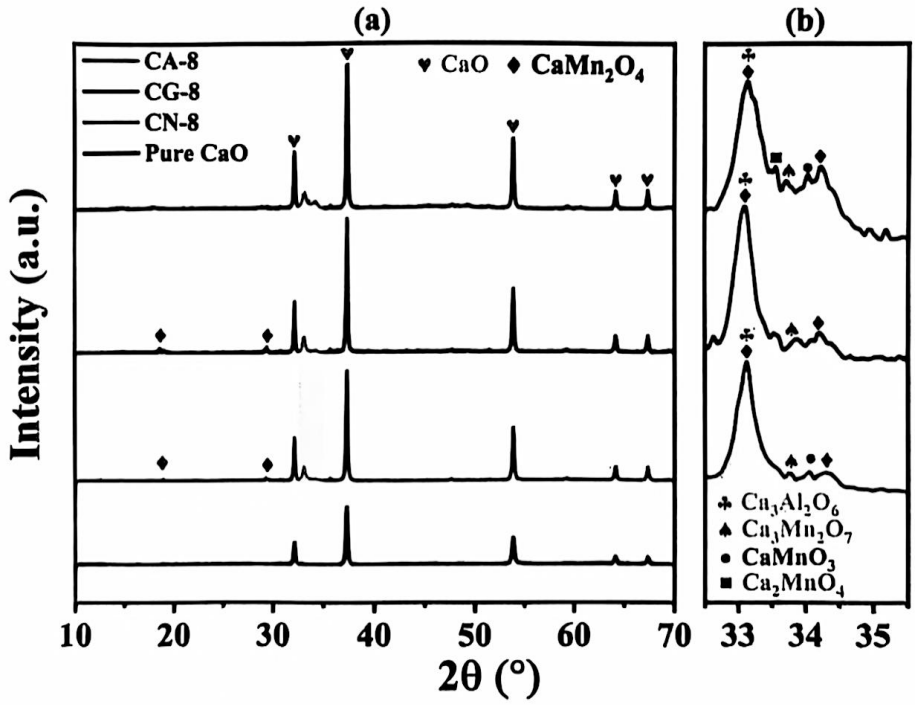

Fig. 5. The XRD patterns of the CaO-based composites with different calcium precursors.

of Ca_2MnO_4 (ICCD 97-007-4344). The disparity in components is probably due to the different difficulties of calcium substrates to produce Ca^{2+} in the hydrolysis reaction, resulting in a deviation in the binding of metal ions to ligands during the polycondensation reaction [37].

Fig. 6 shows XPS spectra of pure CaO and the CaO-based composites, including Ca, O, Mn, and Al elements. Pure CaO has two characteristic peaks at 346.7 eV and 350.2 eV with a binding energy gap of 3.5 eV, representing Ca $2p_{3/2}$ and Ca $2p_{1/2}$ of Ca^{2+} [46]. While for the doped samples, these peaks are located at 347.0 eV and 350.5 eV. For the deconvolution O 1s spectra, the doped samples have an extra peak at 529.0 eV, corresponding to lattice oxygen. After doping the Mn and Al elements, a certain amount of adsorbed oxygen switches to lattice oxygen as shown in Fig. 6(b). The CG-8 sample has the highest proportion of lattice oxygen at 8.75%, and the increase of lattice oxygen is beneficial to promote the migration from active lattice oxygen to oxygen vacancy,

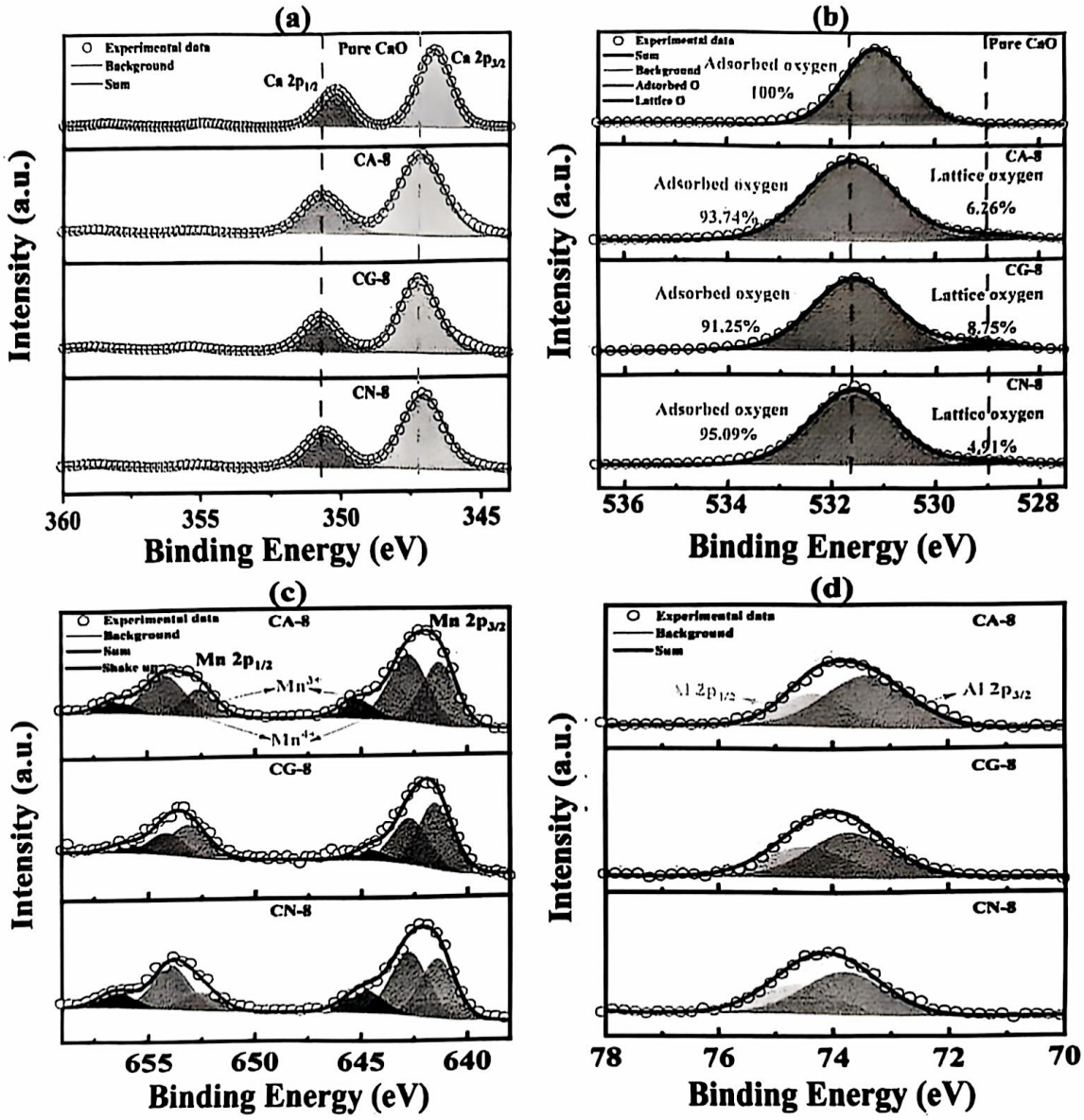

Fig. 6. XPS spectra of pure CaO and the CaO-based composites. (a) Ca 2p. (b) O 1s. (c) Mn 2p. (d) Al 2p.

which enhances the reaction activity and conversion in the carbonation process [25,47]. During the carbonation stage, the Ca atom first transfers electrons to the O atom on the surface layer, and then electrons move from the O_{CaO} to the Cco_2, and finally to the Oco_2 [42]. As shown in Fig. 6(a) and (b), the Ca 2p and O 1s spectra in the doped materials have a shift to higher binding energy compared to pure CaO, which means that Ca atoms and O atoms of the doped materials are easier to transfer electrons to CO_2, accelerating the formation of CO_3^{2-}.

The Mn 2p spectra are presented in Fig. 6(c), where the binding energy gap between Mn $2p_{1/2}$ and Mn $2p_{3/2}$ is approximately 11.5 eV [48]. The peaks at 641.3 eV and 652.6 eV are attributed to Mn^{3+}, while the peaks at 642.8 eV and 654.1 eV belong to Mn^{4+}. The phases with Mn^{3+} or Mn^{4+} can also be observed in XRD results. Moreover, the peaks at 645.4 eV and 656.8 eV are ascribed to shake-up peaks [46,48–51]. The ratio of Mn^{3+}/Mn^{4+} of the CA-8 sample is 0.73 after calculation and the value becomes 0.71 after 20 cycles. The ratios of the other samples are displayed in Table S3. The Al 2p spectra are deconvoluted into two peaks denoting Al $2p_{3/2}$ (73.4 eV) and Al $2p_{1/2}$ (74.4 eV) of Al^{3+}. The XPS spectra of samples after 20 cycles are shown in Fig. S4. The analyses of XPS results indicate that the doping of Mn and Al in CaO changes the crystal structure, contributes to the lattice defect, and induces the generation of lattice oxygen to improve the carbonation reaction.

3.3.2. Optical absorption properties and cyclic test

The optical absorption capacities of calcium-based materials are essential when used in the calcium looping TCES system. Fig. 7(a) displays the spectra absorption of samples, where the CaO-based composites co-doped with Mn and Al effectively promote optical absorption in the wavelength range of 380~2500 nm. As seen in Fig. 7(b), the average optical absorption capacities of CA-8, CG-8, and CN-8 samples are 89.44%, 86.14%, and 73.89%, which are 9.0 times, 8.6 times, and 7.4 times that of pure CaO, respectively. Moreover, the average optical absorption capacities of the doped samples decrease slightly after 20 cycles as shown in Fig. S5, and the attenuation is acceptable within the error range. It is implied that Mn and Al are conducive to increasing the optical absorption capacity of CaO and maintaining excellent light absorption ability.

The cycling results of all samples over 20 cycles are shown in Fig. 8.

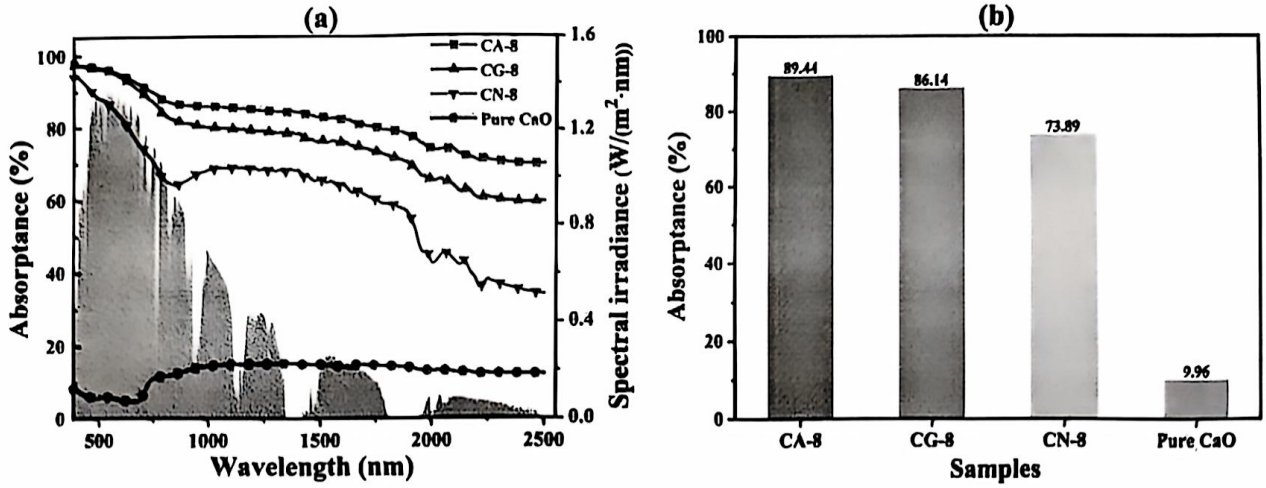

Fig. 7. The optical absorption abilities of CA-8, CG-8, CN-8, and pure CaO. (a) Absorption spectra. (b) The average absorption.

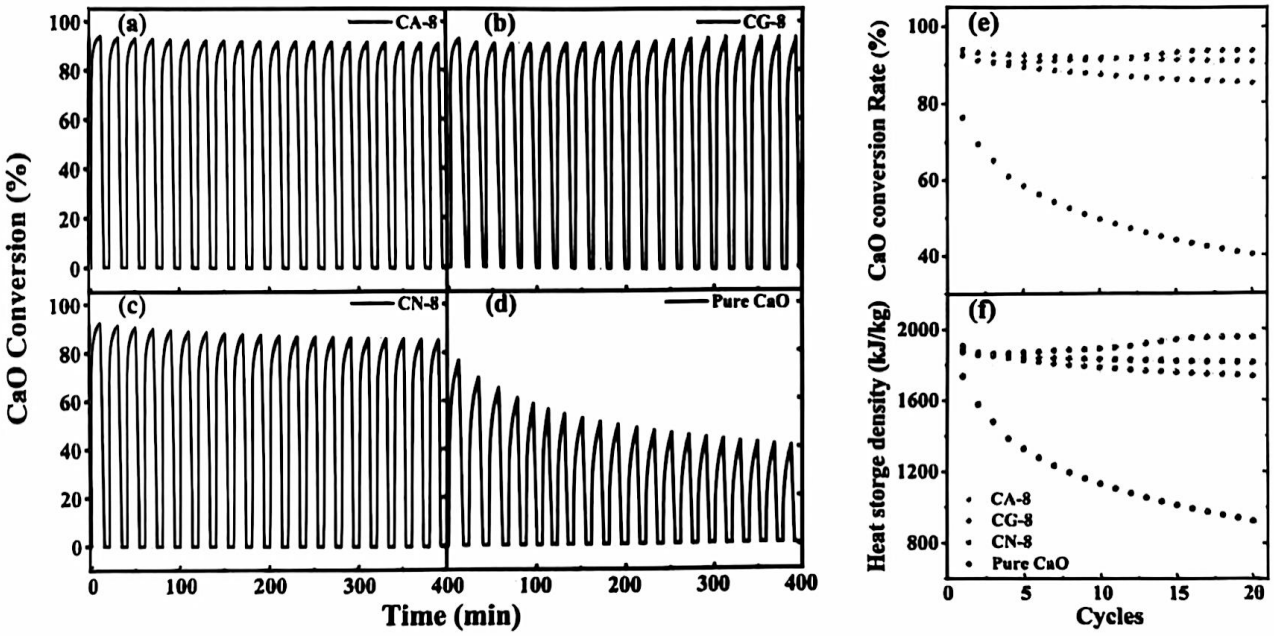

Fig. 8. The cyclic characterization of CA-8, CG-8, CN-8, and pure CaO. (a-d) The thermogravimetric results of samples. (e) The CaO conversion rate of samples. (f) The heat storage density of samples.

As mentioned above, the cyclic performance of the CG-8 sample decreases first and then increases. The CaO conversion rate changes from 92.84% to 93.63% and the heat storage density increases from 1908.16 kJ/kg to 1955.12 kJ/kg, while for other samples, the two critical parameters maintain a downward trend. After 20 cycles, the conversion rates of CA-8, CN-8, and pure CaO decreased by 3.34%, 7.36%, and 36.30%, and the heat storage density of them decreased to 1812.26 kJ/kg, 1736.6 kJ/kg, and 924.92 kJ/kg, respectively. The CO_2 adsorption capacities of all samples during 20 cycles are displayed in Fig. S6, whose changing trend is consistent with that of heat storage density. It demonstrates that the composites co-doped with Mn and Al exhibit excellent cycling stability compared to pure CaO whatever calcium precursors are used. While for pure CaO, the rapid decline in performance is closely related to its severe sintering at high temperatures.

3.3.3. Microstructure analysis

The particle size distributions of samples are shown in Fig. S7. The particle size ranges of the four samples are 169.8 nm–197.9 nm (Pure CaO), 53.4 nm–89.9 nm (CA-8), 43.5 nm–108.2 nm (CG-8), and 43.4 nm–107.0 nm (CN-8). Pure CaO has the largest average particle size (189.5 nm) in Table S4, which is probably attributed to the large particle size of commercial $CaCO_3$. The average particle size of CA-8, CG-8, and CN-8 is 71.9 nm, 69.2 nm, and 69.6 nm, respectively. Combined with the sound-assisted fluidization technology proposed by Ammendola and Raganati et al. [52,53], calcium-based fine powder has the potential to be directly applied to fluidized beds.

To analyze the pore characteristics, the N_2 adsorption-desorption isotherms and pore diameter distributions of samples are displayed in Fig. 9. The specific surface area and pore volume of all samples are listed in Table 1. The isotherms of the Mn and Al co-doped composites are attributed to type IV according to the IUPAC classification and the

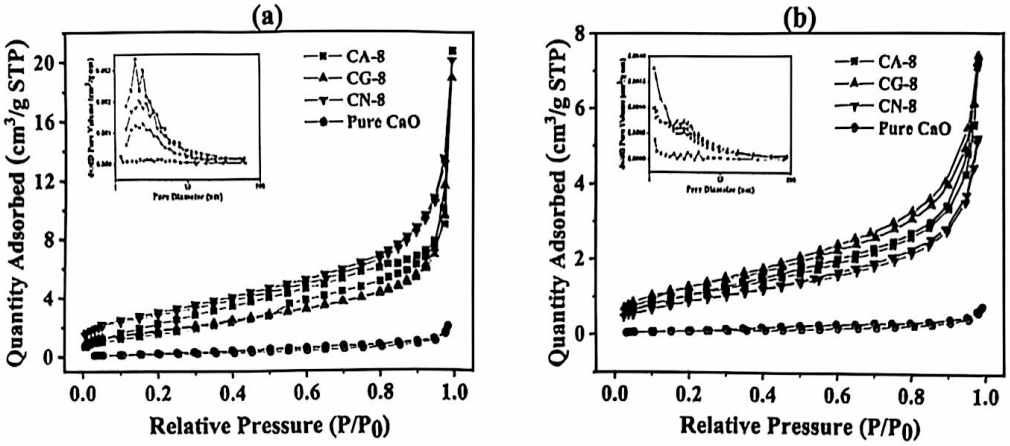

Fig. 9. N_2 adsorption-desorption isotherms and pore diameter distributions (inset) of CA-8, CG-8, CN-8, and pure CaO. (a) Fresh samples. (b) Samples after 20 cycles.

Table 1
BET surface area and BJH pore volume of the CaO-based materials before and after 20 cycles.

Samples	Surface area (m^2/g)	Pore volume (cm^3/g)
Pure CaO	0.701	0.003
Pure CaO after 20 cycles	0.309	0.001
CA-8	8.764	0.033
CA-8 after 20 cycles	6.894	0.012
CG-8	8.488	0.030
CG-8 after 20 cycles	7.283	0.014
CN-8	13.978	0.032
CN-8 after 20 cycles	5.551	0.012

hysteresis loop belongs to type H3 [23,54]. It means that the doped materials are mesoporous materials with slit-like pores. However, the isotherm of pure CaO is type II, corresponding to a typical nonporous material. From the pore diameter distributions, the mesopores of the doped materials are concentrated in the range of 2~10 nm before and after the cyclic test, while pure CaO has almost no pores.

As shown in Fig. 10, the morphologies of fresh samples and those after 20 cycles are monitored via SEM images. The CaO-based materials synthesized from different calcium precursors show various structures. Initial pure CaO and that after 20 cycles all present a dense blocky structure, verifying its low BET and BJH values as summarized in Table 1. It is the reason for the poor cycling stability of pure CaO. Moreover, growth and accumulation of the product layer are also observed in Fig. 10(e) [55]. The fresh sample of CA-8 is composed of microparticles as shown in Fig. 10(b). The microparticles were agglomerated and fused after 20 cycles, resulting in the disappearance of pores and a drop in pore volume from 0.033 cm^3/g to 0.012 cm^3/g. For the CG-8 sample, a skeleton with abundant pores formed as shown in Fig. 10(c). The porous skeleton is still stable after 20 cycles, which inhibits the coalescence of CaO particles and promotes CO_2 diffusion into the inside of particles. The BET value of the CG-8 sample has a slight drop from 8.488 m^2/g to 7.283 m^2/g, maintaining excellent cycling stability. Compared with the CA-8 and CG-8 samples, the CN-8 sample has a sponge-like network structure that is densified after cycles. The grains grew and fused as shown in Fig. 10(h). Along with the process of densification, the BET value of the CN-8 sample dramatically decreases from 13.978 m^2/g to 5.551 m^2/g, and its BJH value decreases from 0.032 cm^3/g to 0.012 cm^3/g, proving the fact that the CN-8 sample has the worst cycling stability among the three doped samples.

The TEM images of samples after 20 cycles are shown in Fig. S8. The particles of the CG-8 sample tend to connect with each other after cycles, forming nets. This interesting phenomenon is not observed in other samples. The formation of nets in particles may be related to the increase in the energy storage density of the CG-8 sample. The formation of nets may create new grain boundaries and porosity inside the particles [26], which is beneficial to the mass transfer process and improves the cyclic performance.

The porous structures of composites are generated by the decomposition of calcium precursors and the generation of gases [38]. The

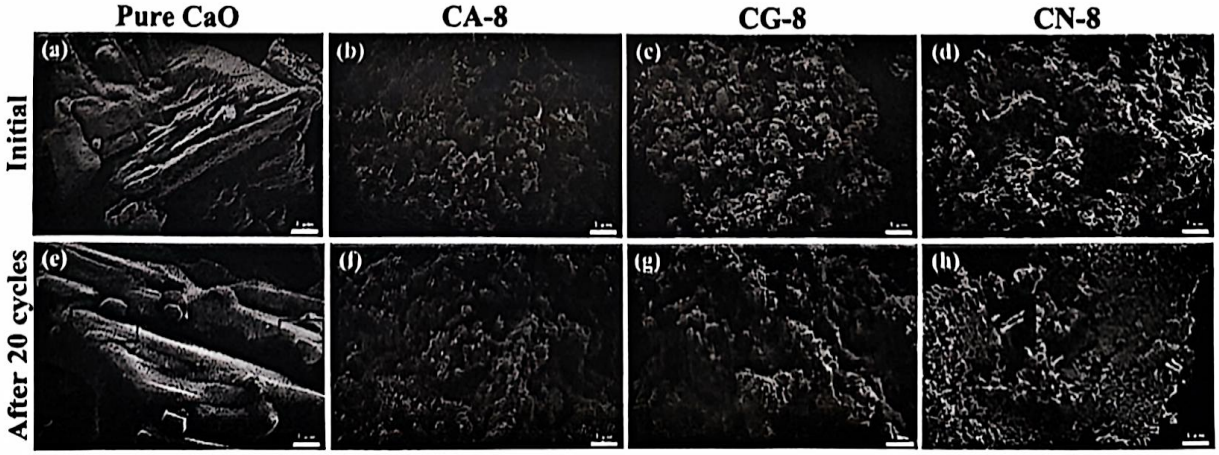

Fig. 10. Morphologies of all samples. Pure CaO, (a) fresh sample, (e) after the 20th cycle; CA-8, (b) fresh sample, (f) after the 20th cycle; CG-8, (c) fresh sample, (g) after the 20th cycle; CN-8, (d) fresh sample, (h) after the 20th cycle.

cyclic performance difference of CaO-based composites results from the pore richness and the stability of the porous skeleton. Compared with calcium nitrate and calcium acetate, calcium gluconate dramatically decomposed at 201 °C generating large amounts of CO_2. The escape of CO_2 results in abundant pores, which can be maintained for a long time under the synergistic stability of Mn and Al. Therefore, the CaO-based composites prepared from calcium gluconate have a longer cycle life and better heat storage performance.

3.3.4. The long-term cyclic performance

To exploit potentialities for the doped samples during long cycles, 60 cycles of the thermogravimetric test were carried out, and the conditions were consistent with those of 20 cycles. Fig. 11 shows the CaO conversion rate of four samples in the 1st cycle, the 20th cycle, the 40th cycle, and the 60th cycle. As displayed in Fig. 11, the conversion rate of pure CaO decreases to 16.93% over 60 cycles, indicating that the material is seriously sintered. The modified composites still exhibit excellent cyclic performance. Among them, the conversion rate of the CG-8 sample is as high as 91.50%, which is only 1.32% lower than that of the first cycle. The conversion rate of the CA-8 sample remains at 87.08%, which is higher than that of CN-8 (76.96%). As shown in Fig. S9, the porous skeleton structure of the CG-8 sample remains stable after 60 cycles. CA-8 and CN-8 samples have signs of sintering, but some pores still exist. The sintering of pure CaO is serious, and the small grains are fused with the large grains. After 60 cycles, the conversion rates of the three doped samples are 5.40 times, 5.14 times, and 4.55 times higher than the value of pure CaO, respectively. It shows that the doping of Mn and Al elements effectively prevents the severe sintering of CaO at high temperatures and ensures efficient and durable performance. Therefore, the doped samples, especially the CG-8 sample, meet the requirements of the calcium looping TCES system and have the potential for application.

3.4. Analysis of the DFT calculations

The above results confirm that the CO_2 capture ability and the cycling stability of the CaO-based materials are improved after the doping atoms enter the CaO lattice. To further explain the mechanism of the dopants, the adsorption energies on the pure CaO surface and the CaO surface co-doped with Mn and Al were calculated and some key parameters were listed in Table 2. A variety of configurations are generated on the doped CaO surface. The configuration with the lowest formation energy is selected for subsequent calculations. Compared with the perfect CaO (100) surface in Fig. 12(a), the doped CaO (100) surface

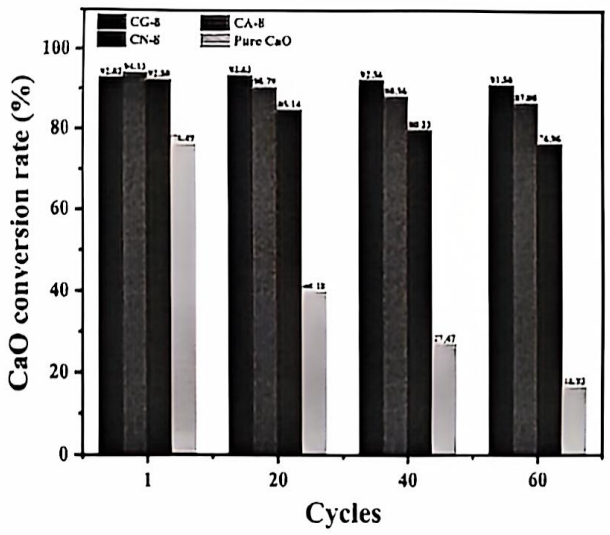

Fig. 11. The CaO conversion rates of CA-8, CG-8, CN-8, and pure CaO in the 1st cycle, the 20th cycle, the 40th cycle, and the 60th cycle.

Table 2
The calculation results of adsorption energies and bond lengths.

Configuration	Adsorption sites	$d(Cco_2\text{-}Oco_2)$ (Å)	$d(Cco_2\text{-}Ocao)$ (Å)	E_{ads} (eV)
Mn-Al-CaO (100)	I	1.260/1.259	1.424	-3.356
	II	1.248/1.280	1.391	-3.634
	III	1.277/1.258	1.390	-3.773
	IV	1.273/1.271	1.369	-2.827
	V	1.266/1.255	1.417	-3.099
	VI	1.245/1.270	1.429	-3.816
CaO (100)		1.267/1.266	1.492	-1.567

causes occurs collapse, which results from the difference in the charged quantity among Mn, Al, and Ca atoms. The atomic collapse generates a steady structure to maintain the minimum energy.

The geometry of the CaO surface combined with CO_2 was optimized as shown in Fig. 13(a). A new bond with a length of 1.492 Å is generated between Cco_2 and O_{CaO}, and the angle of O-C-O (CO_2) changes from 180° to 129.047°. The adsorption energy is -1.567 eV calculated by Eq. (5). As analyzed in Fig. 12(b), Six oxygen adsorption sites (I ~ VI) are identified based on the stable configuration of the doped CaO surface. The relative results of CO_2 adsorbed on the defective CaO surface are summarized in Table 2. For the six adsorption sites, the maximum adsorption energy is at site VI, reaching -3.816 eV, which is 2.4 times higher than that of the pure CaO surface. Even the minimum adsorption energy is 1.8 times higher than the value on the pure CaO surface and the bond length of the Cco_2-Ocao at six sites is all shorter than that of the pure CaO surface, suggesting that the lattice distortion enhances the CO_2 capture ability and the binding strength of CO_2. The change in the CO_2 uptake rate (R_N) with time is shown in Fig. S10, which also proves the doped samples are better than pure CaO in terms of CO_2 adsorption, especially in the stage controlled by chemical reaction.

The configuration that CO_2 adsorbed on site VI is optimized as shown in Fig. 13(b), where the two Cco_2-Oco_2 bonds display different lengths. The bond close to the Mn atom exhibits a length of 1.245 Å, shorter than that far away from the Mn atom (1.270 Å). This situation can be caused by the weakened electrostatic interaction between the Mn atom and Oco_2 after the lattice distortion, increasing the binding strength between Cco_2 and Oco_2.

4. Conclusion

In this work, we choose calcium acetate, calcium gluconate, and calcium nitrate as calcium precursors to synthesize CaO-based thermochemical heat storage materials that are co-modified with Mn and Al. After the initial exploratory experiment, the optimum reaction temperature (750 °C–750 °C) for the cyclic test is determined. After the thermogravimetric test and the spectral absorption test, the optimal doping ratio is determined to be Ca: Mn: Al = 100: 8: 8. The average optical absorption rates of the synthesized CA-8, CG-8, and CN-8 samples are 89.44%, 86.14%, and 73.89%, while that of pure CaO is only 9.96%. The CG-8 sample has the best cycling stability. Its conversion rate of CaO maintains at 91.50% over 60 cycles, which is 5.40 times that of pure CaO. Moreover, the CA-8 sample (87.08%) and the CN-8 sample (76.96%) are 5.14 times and 4.55 times that of pure CaO, respectively. Compared with the CA-8 and CN-8 samples, the CG-8 sample generates a stable skeleton and maintains a porous structure after cycles, which is the reason for its excellent performance. The adsorption energies of CO_2 adsorbed on the pure CaO surface and the defect surface co-doped with Mn and Al are calculated by DFT. Compared with the perfect CaO surface, the defect surface is easier to capture CO_2, and the generated Cco_2-O_{CaO} bond strength is higher. These results explain the promotion effect of Mn and Al doping on the as-prepared materials from the theoretical level and benefit understanding the mechanism of doping elements on the improvement of CaO-based TCES materials.

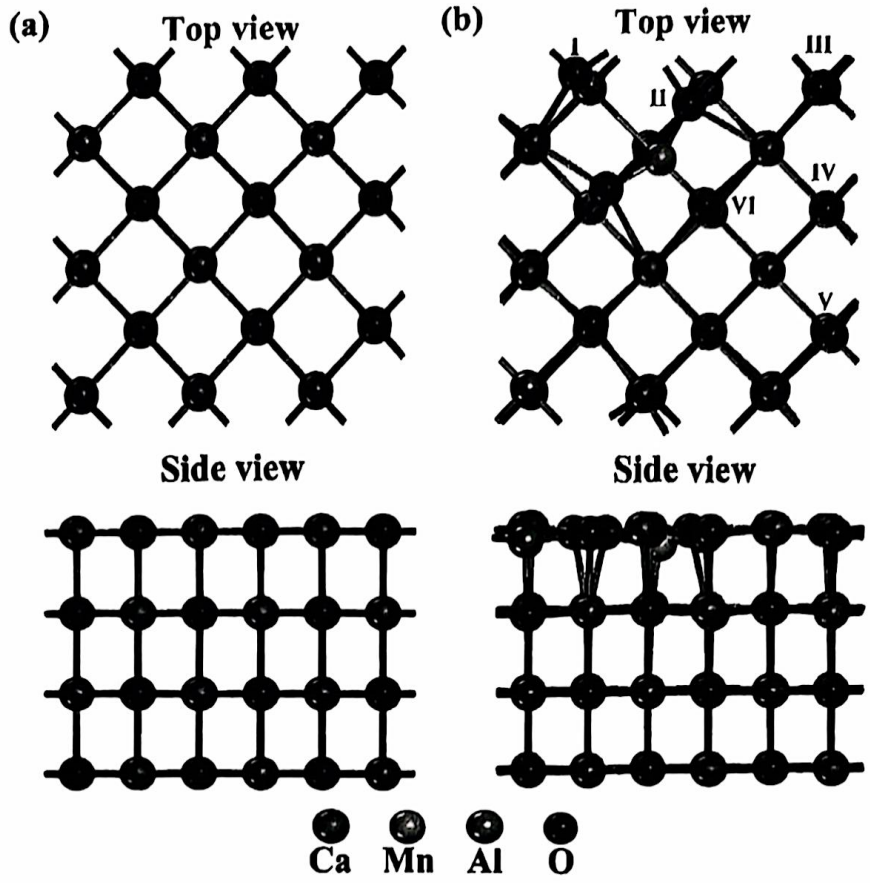

Fig. 12. The top view and side view of geometric structures after optimization. (a) CaO (100) surface. (b) The CaO (100) surface co-doped with Mn and Al.

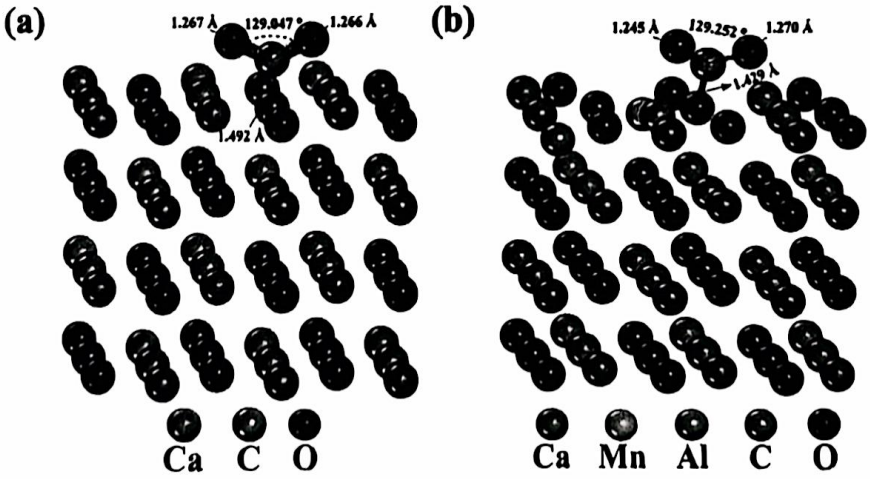

Fig. 13. (a) Geometry optimization of CO_2 adsorption on the CaO surface. (b) Geometry optimization of CO_2 adsorption on the doped CaO surface (site VI).

CRediT authorship contribution statement

Fengyuan Chai: Writing – review & editing, Visualization, Investigation, Formal analysis, Conceptualization. **Peiwang Zhu:** Writing – review & editing, Validation. **Haoran Xu:** Writing – review & editing, Formal analysis. **Xiangyu Xie:** Writing – review & editing, Data curation. **Gang Xiao:** Writing – review & editing, Supervision, Project administration, Funding acquisition.

Declaration of competing interest

The authors declare that they have no known competing financial interests or personal relationships that could have appeared to influence the work reported in this paper.

Data availability

Data will be made available on request.

Acknowledgements

The authors gratefully acknowledge the financial support from the National Key Research and Development Program of China Grant (No. 2021YFF0500403), Key R&D Program of Zhejiang (No. 2022C01043) and the Fundamental Research Funds for the Central Universities (2022ZFJH04).

Appendix A. Supplementary data

Supplementary data to this article can be found online at https://doi.org/10.1016/j.solmat.2024.112761.

References

[1] A. Shahsavari, M. Akbari, Potential of solar energy in developing countries for reducing energy-related emissions, Renew. Sustain. Energy Rev. 90 (2018) 275–291.
[2] A.J. Carrillo, J. González-Aguilar, M. Romero, J.M. Coronado, Solar energy on demand: a review on high temperature thermochemical heat storage systems and materials, Chem. Rev. 119 (2019) 4777–4816.
[3] W. Ding, T. Bauer, Progress in research and development of molten chloride salt technology for next generation concentrated solar power plants, Engineering 7 (2021) 334–347.
[4] K. Vignarooban, X. Xu, A. Arvay, K. Hsu, A.M. Kannan, Heat transfer fluids for concentrating solar power systems – a review, Appl. Energy 146 (2015) 383–396.
[5] M.T. Islam, N. Huda, A.B. Abdullah, R. Saidur, A comprehensive review of state-of-the-art concentrating solar power (CSP) technologies: current status and research trends, Renew. Sustain. Energy Rev. 91 (2018) 987–1018.
[6] J.M. Valverde, The Ca-looping process for CO_2 capture and energy storage: role of nanoparticle technology, J. Nanoparticle Res. 20 (2018) 1–16.
[7] R. Chacartegui, A. Alovisio, C. Ortiz, J.M. Valverde, V. Verda, J.A. Becerra, Thermochemical energy storage of concentrated solar power by integration of the calcium looping process and a CO_2 power cycle, Appl. Energy 173 (2016) 589–605.
[8] C. Ortiz, M.C. Romano, J.M. Valverde, M. Binotti, R. Chacartegui, Process integration of Calcium-Looping thermochemical energy storage system in concentrating solar power plants, Energy 155 (2018) 535–551.
[9] C. Ortiz, J.M. Valverde, R. Chacartegui, L.A. Perez-Maqueda, P. Gimenez, The Calcium-Looping ($CaCO_3$/CaO) process for thermochemical energy storage in Concentrating Solar Power plants, Renew. Sustain. Energy Rev. 113 (2019) 109252.
[10] M. Benitez-Guerrero, J.M. Valverde, P.E. Sanchez-Jimenez, A. Perejon, L.A. Perez-Maqueda, Calcium-Looping performance of mechanically modified Al_2O_3-CaO composites for energy storage and CO_2 capture, Chem. Eng. J. 334 (2018) 2343–2355.
[11] S. Stendardo, L.K. Andersen, C. Herce, Self-activation and effect of regeneration conditions in CO_2-carbonate looping with CaO-$Ca_{12}Al_{14}O_{33}$ sorbent, Chem. Eng. J. 220 (2013) 383–394.
[12] H.R. Radfarnia, A. Sayari, A highly efficient CaO-based CO_2 sorbent prepared by a citrate-assisted sol–gel technique, Chem. Eng. J. 262 (2015) 913–920.
[13] X. Chen, X. Jin, Z. Liu, X. Ling, Y. Wang, Experimental investigation on the CaO/$CaCO_3$ thermochemical energy storage with SiO_2 doping, Energy 155 (2018) 128–138.
[14] R. Han, J. Gao, S. Wei, Y. Su, C. Su, J. Li, Q. Liu, Y. Qin, High-performance CaO-based composites synthesized using a space-confined chemical vapor deposition strategy for thermochemical energy storage, Sol. Energy Mater. Sol. Cells 206 (2020) 110346.
[15] R. Koirala, K.R. Gunugunuri, S.E. Pratsinis, P.G. Smirniotis, Effect of zirconia doping on the structure and stability of CaO-based sorbents for CO_2 capture during extended operating cycles, J. Phys. Chem. C 115 (2011) 24804–24812.
[16] L. Li, D.L. King, Z. Nie, C. Howard, Magnesia-stabilized calcium oxide absorbents with improved durability for high temperature CO_2 capture, Ind. Eng. Chem. Res. 48 (2009) 10604–10613.
[17] K. Wang, F. Gu, P.T. Clough, P. Zhao, E.J. Anthony, Porous MgO-stabilized CaO-based powders/pellets via a citric acid-based carbon template for thermochemical energy storage in concentrated solar power plants, Chem. Eng. J. 390 (2020) 124163.
[18] C. Li, Y. Li, C. Zhang, Y. Dou, Z. He, J. Zhao, CaO/$CaCO_3$ thermochemical energy storage performance of high-alumina granule stabilized papermaking soda residue, Fuel Process. Technol. 237 (2022) 107444.
[19] H. Li, Y. Chen, L. Leng, Y. Hu, Thermochemical energy storage of concentrated solar power by novel Y_2O_3-doped CaO pellets, Energy Fuels 35 (2021) 12610–12618.
[20] P. Ammendola, F. Raganati, F. Miccio, A.N. Murri, E. Landi, Insights into utilization of strontium carbonate for thermochemical energy storage, Renew. Energy 157 (2020) 769–781.
[21] P. Ammendola, F. Raganati, E. Landi, A. Natali Murri, F. Miccio, Kinetics of the carbonation reaction of an SrO-Al_2O_3 composite for thermochemical energy storage, Chem. Eng. J. 420 (2021) 129618.
[22] Y. Hu, W. He, J. Cao, G. Cheng, R. Fu, L. Huang, Decorating CaO with dark Co_2MnO_4 for direct solar thermal conversion and stable thermochemical energy storage, Sol. Energy Mater. Sol. Cells 248 (2022) 111977.
[23] J. Sun, S. Bai, K. Li, Y. Zhou, Y. Chen, L. Liu, Z. Zhou, Evaluation of thermochemical energy storage performance of Fe-/Mn-doped, Zr-stabilized, CaO-based composites under different thermal energy storage modes, ACS Appl. Energy Mater. 5 (2022) 4903–4915.
[24] X. Wang, X. Liu, H. Zheng, C. Song, K. Gao, C. Tian, N. Sun, Z. Jiang, Hierarchically doping calcium carbonate pellets for directly solar-driven high-temperature thermochemical energy storage, Sol. Energy 251 (2023) 197–207.
[25] Y. Da, J. Zhou, Microscopic mechanisms of Mn-doped $CaCO_3$ heat carrier with enhanced optical absorption and accelerated decomposition kinetics for directly storing solar energy, Sol. Energy Mater. Sol. Cells 250 (2023) 112103.
[26] H. Liu, J. Zhang, J. Wei, Mn and Mg synergistically stabilized CaO as an effective thermochemical material for solar energy storage, Sol. Energy Mater. Sol. Cells 252 (2023) 112202.
[27] L. Teng, Y. Xuan, Y. Da, X. Liu, Y. Ding, Modified Ca-Looping materials for directly capturing solar energy and high-temperature storage, Energy Storage Mater. 25 (2020) 836–845.
[28] H. Zheng, C. Song, C. Bao, X. Liu, Y. Xuan, Y. Li, Y. Ding, Dark calcium carbonate particles for simultaneous full-spectrum solar thermal conversion and large-capacity thermochemical energy storage, Sol. Energy Mater. Sol. Cells 207 (2020) 110364.
[29] Y. Da, J. Zhou, Multi-doping strategy modified calcium-based materials for improving the performance of direct solar-driven calcium looping thermochemical energy storage, Sol. Energy Mater. Sol. Cells 238 (2022) 111613.
[30] Y. Da, J. Zhou, F. Zeng, Calcium-based composites directly irradiated by solar spectrum for thermochemical energy storage, Chem. Eng. J. 456 (2023) 140986.
[31] B. Sarrión, A. Perejón, P.E. Sánchez-Jiménez, L.A. Pérez-Maqueda, J.M. Valverde, Role of calcium looping conditions on the performance of natural and synthetic Ca-based materials for energy storage, J. CO_2 Util. 28 (2018) 374–384.
[32] J.D. Durán-Martín, P.E. Sánchez Jimenez, J.M. Valverde, A. Perejón, J. Arcenegui-Troya, P. García Triñanes, L.A. Pérez Maqueda, Role of particle size on the multicycle calcium looping activity of limestone for thermochemical energy storage, J. Adv. Res. 22 (2020) 67–76.
[33] M. Benitez-Guerrero, B. Sarrion, A. Perejon, P.E. Sanchez-Jimenez, L.A. Perez-Maqueda, J. Manuel Valverde, Large-scale high-temperature solar energy storage using natural minerals, Sol. Energy Mater. Sol. Cells 168 (2017) 14–21.
[34] Q. Li, H. Wu, Z. Wang, J. Wang, Analysis and optimal design of membrane processes for flue gas CO_2 capture, Sep. Purif. Technol. 298 (2022) 121584.
[35] Y. Xu, B. Lu, C. Luo, F. Wu, X. Li, L. Zhang, Na_2CO_3 promoted CaO-based heat carrier for thermochemical energy storage in concentrated solar power plants, Chem. Eng. J. 435 (2022) 134852.
[36] Y. Xu, T. Zhang, B. Lu, C. Luo, F. Wu, X. Li, L. Zhang, Glycine tailored effective CaO-based heat carriers for thermochemical energy storage in concentrated solar power plants, Energy Convers. Manag. 250 (2021) 114886.
[37] C. Luo, Y. Zheng, C. Zheng, J. Yin, C. Qin, B. Feng, Manufacture of calcium-based sorbents for high temperature cyclic CO_2 capture via a sol–gel process, Int. J. Greenh. Gas Control 12 (2013) 193–199.
[38] L. Jiang, S. Hu, S.S.A. Syed-Hassan, Y. Wang, C. Shuai, S. Su, C. Liu, H. Chi, J. Xiang, Performance and carbonation kinetics of modified CaO-based sorbents derived from different precursors in multiple CO_2 capture cycles, Energy Fuels 30 (2016) 9563–9571.
[39] M.C. Payne, M.P. Teter, D.C. Allan, T.A. Arias, J.D. Joannopoulos, Iterative minimization techniques for *ab initio* total-energy calculations: molecular dynamics and conjugate gradients, Rev. Mod. Phys. 64 (1992) 1045–1097.
[40] J.P. Perdew, K. Burke, M. Ernzerhof, Generalized gradient approximation made simple, Phys. Rev. Lett. 77 (1996) 3865–3868.
[41] W. Dai, Z.-H. Shui, K. Li, First-principle investigations of CaO (100) surface and adsorption of H_2O on CaO (100), Comput. Theor. Chem. 967 (2011) 185–190.
[42] Z. Sun, J. Wang, W. Du, G. Lu, P. Li, X. Song, J. Yu, Density functional theory study on the thermodynamics and mechanism of carbon dioxide capture by CaO and CaO regeneration, RSC Adv. 6 (2016) 39460–39468.
[43] D. Kong, M. Ji, Q. Chen, Y. Zhang, B. Nie, Influence of doping Fe on performance of calcium-based doped materials for thermochemical energy storage: a DFT study, Phys. B Condens. Matter 638 (2022) 413956.
[44] A. Naskar, S. Paul, Non-destructive measurement of grinding-induced deformation-depth using grazing incidence X-ray diffraction technique, NDT E Int. 126 (2022) 102592.
[45] V. Manovic, E.J. Anthony, Thermal activation of CaO-based sorbent and self-reactivation during CO_2 capture looping cycles, Environ. Sci. Technol. 42 (2008) 4170–4174.
[46] T. Wang, X. Qian, D. Yue, X. Yan, H. Yamashita, Y. Zhao, $CaMnO_3$ perovskite nanocrystals for efficient peroxydisulfate activation, Chem. Eng. J. 398 (2020) 125638.
[47] D. Xiang, C. Gu, H. Xu, G. Xiao, Self-assembled structure evolution of Mn-Fe oxides for high temperature thermochemical energy storage, Small 17 (2021) 2101524.
[48] G. Huang, C. Wang, C. Yang, P. Guo, H. Yu, Degradation of bisphenol A by peroxymonosulfate catalytically activated with $Mn_{1.8}Fe_{1.2}O_4$ nanospheres: synergism between Mn and Fe, Environ. Sci. Technol. 51 (2017) 12611–12618.
[49] W. Si, Y. Wang, S. Zhao, F. Hu, J. Li, A facile method for in situ preparation of the MnO_2 /$LaMnO_3$ catalyst for the removal of toluene, Environ. Sci. Technol. 50 (2016) 4572–4578.
[50] Q. Tang, L. Jiang, J. Liu, S. Wang, G. Sun, Effect of surface manganese valence of manganese oxides on the activity of the oxygen reduction reaction in alkaline media, ACS Catal. 4 (2014) 457–463.
[51] S. Ponce, M.A. Peña, J.L.G. Fierro, Surface properties and catalytic performance in methane combustion of Sr-substituted lanthanum manganites, Appl. Catal. B Environ. 24 (2000) 193–205.

[52] F. Raganati, R. Chirone, P. Ammendola, Calcium-looping for thermochemical energy storage in concentrating solar power applications: evaluation of the effect of acoustic perturbation on the fluidized bed carbonation, Chem. Eng. J. 392 (2020) 123658.
[53] F. Raganati, P. Ammendola, Sound-assisted fluidization for temperature swing adsorption and calcium looping: a review, Materials 14 (2021) 672.
[54] M. Thommes, K. Kaneko, A.V. Neimark, J.P. Olivier, F. Rodriguez-Reinoso, J. Rouquerol, K.S.W. Sing, Physisorption of gases, with special reference to the evaluation of surface area and pore size distribution (IUPAC Technical Report), Pure Appl. Chem. 87 (2015) 1051–1069.
[55] J.C. Abanades, D. Alvarez, Conversion limits in the reaction of CO_2 with lime, Energy Fuels 17 (2003) 308–315.